Qualitative and quantitative comparison of RANS simulation results for a 7 element GOX/GCH_4 rocket combustor

Nikolaos Perakis* and Oskar J. Haidn†
Chair of Turbomachinery and Flight Propulsion, Technical University of Munich, Boltzmannstr. 15, 85748 Garching, Germany

Daniel Rahn‡ and Daniel Eiringhaus§
ArianeGroup GmbH, Robert-Koch-Str. 1, 82024 Taufkirchen, Germany

Silong Zhang ¶
Institute of Advanced Power, Harbin Institute of Technology, No.92 West Da-Zhi Street, 150001, Harbin, China

Yu Daimon‖
Research and Development Directorate, Japan Aerospace Exploration Agency, 2-1-1 Sengen, Tsukuba, Ibaraki, Japan

Sebastian Karl** and Tim Horchler††
German Aerospace Center (DLR), Institute of Aerodynamics and Flow Technology, Göttingen, Germany

The present study aims at comparing the different methodologies used in the modeling and simulation of combustion and heat transfer in rocket thrust chambers. Different approaches were implemented by five different groups within the framework of the SFB-TRR 40 Summer Program 2017, in order to simulate the flow and combustion inside a multi-element rocket combustor, operated with gaseous oxygen (GOX) and gaseous methane (GCH_4). The test results provided for the validation of the different techniques, were obtained by experiments run at the Chair of Turbomachinery and Flight Propulsion of the Technical University of Munich (TUM). All five different approaches were based on RANS models for turbulence and turbulence-chemistry interaction (TCI) and the corresponding results were evaluated based on their agreement with the experimental data. The main focus was placed on the pressure and heat flux profiles along the thrust chamber wall and all methods were able to qualitatively capture the experimental trends. Significant differences were observed regarding the azimuthal variation of heat flux at the chamber wall. The secondary flows and the injector-injector interaction were identified as the primary culprits for the measured deviations. However, due to the absence of experimental data, the validity of this azimuthal variation could not be evaluated.

I. Nomenclature

p	=	pressure
Pr_t	=	turbulent Prandtl number
$\dot{q}$	=	heat flux
Sc_t	=	turbulent Schmidt number
T	=	temperature
x	=	axial position

*Graduate Student, Technical University of Munich, nikolaos.perakis@ltf.mw.tum.de.
†Prof. Dr.-Ing., Technical University of Munich
‡Graduate Student, Technical University of Munich
§Graduate Student, ArianeGroup GmbH
¶Associate Professor, Harbin Institute of Technology
‖Research Engineer, Japan Aerospace Exploration Agency
**Research Engineer, Spacecraft Department, German Aerospace Center
††Research Engineer, Spacecraft Department, German Aerospace Center

y^+ = dimensionless wall distance
Z_{st} = stoichiometric mixture fraction
θ = angle

II. Introduction

A very important step in the process of designing and optimizing new components or subsystems for rocket propulsion devices is the numerical simulation of the flow and combustion in them. Implementing CFD tools in the early design process significantly reduces the development time and cost and allows for greater flexibility. Furthermore, CFD tools can be very useful in interpreting experimental data, since they give insight into the mixing, energy release and heat transfer to the wall, which are not always available to the experimenter.

The reliability of a numerical tool lies in accurately describing the physical and chemical processes taking place within the thrust chamber. This is done by a set of models (and the corresponding numerical methods to solve them), which must be validated for the wide range of operating conditions that can occur in different types of rocket engines. For that reason, a significant step during the development of numerical tools for combustion and turbulence modeling in rocket engines is the validation of the models. Within this framework the Chair of Turbomachinery and Flight Propulsion (LTF) at the Technical University of Munich (TUM) has tested several different configurations of rocket combustors and propellant combinations, building an experimental data base which can be used in the validation process. As part of the SFB-TRR 40 Summer Program 2017 a test case from this data base was defined. The experimental rocket combustor is operated with gaseous oxygen (GOX) and gaseous methane (GCH_4) and has a multi-element injector. A detailed description of the test campaign can be found in Silvestri et al. [1].

In the present paper the numerical results of four separate groups are shown and compared to each other. Results from the Chair of Turbomachinery and Flight Propulsion of the Technical University of Munich (TUM), from ArianeGroup, from Harbin Institute of Technology (HIT), from the Japan Aerospace Exploration Agency (JAXA) and from the Institute of Aerodynamics and Flow Technology of the German Aerospace Center (DLR) are presented. All groups performed 3D RANS simulations of the flow and combustion in the chamber. Purpose of the study was to evaluate the various numerical approaches used in industry and academia regarding the simulation of rocket engines, assess their differences and interpret the corresponding results.

III. Test case description

In the context of the national research program Transregio SFB-TRR 40 on "Technological Foundation for the design of thermally and mechanically high loaded components of Future Space Transportation System", the examined multi-injector combustion chamber was designed for GOX and GCH_4 allowing high chamber pressures (up to 100 bar) and film cooling behavior examination. One of the key aspects of the project is to improve the knowledge on heat transfer processes and cooling methods in the combustion chamber, which is mandatory for the engine design. The attention is focused, in particular, on injector-injector and injector-wall interaction. In order to have a first characterization of the injectors' behavior, the multi-element combustion chamber is tested at low combustion chamber pressures and for a wide range of mixture ratios [1].

The seven-element rocket combustion chamber has an inner diameter of 30 mm and a contraction ratio of 2.5 in order to achieve Mach numbers similar to the ones in most rocket engine applications. The combustion chamber, depicted in Fig. 1, consists of four cylindrical water cooled chamber segments, as well as a nozzle segment (individually cooled), adding up to a total length of 382 mm. For the current study, shear coaxial injector elements are integrated. The test configuration includes the GOX post being mounted flush with respect to the injection face. For the present test case an operating point with mean combustion chamber pressure of 18.3 bar and mixture ratio of 2.65 was chosen. The experimental data made available for the numerical simulations included the mass flow rates of oxygen and methane, the wall temperature, pressure profile and integral heat flux values. For the determination of the heat flux values in the four chamber segments (A-D) and the nozzle (N), a calorimetric method is applied. The average heat flux of each chamber segment is determined by the enthalpy difference of the coolant between inlet and outlet. This is obtained by precise temperature measurements in the water manifolds between the test segments.

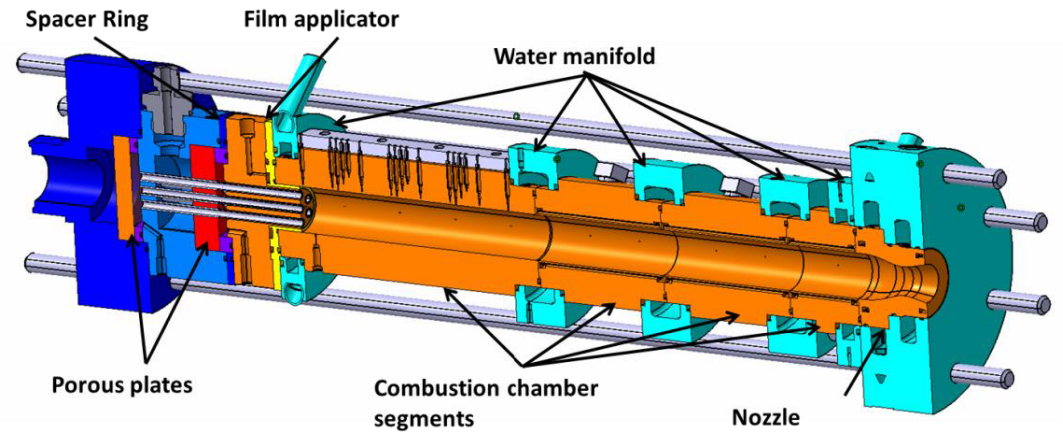

Fig. 1 Sketch of the combustion chamber

IV. Computational setups

The following section outlines the individual setups and numerical models used in each approach. All of the five groups performed 3D RANS simulations using commercial or in-house tools. In the case of TUM and HIT, the commercial solver ANSYS Fluent was used, whereas the JAXA group utilized CRUNCH-CFD for their calculations and the in-house tools Rocflam3 and TAU were used by ArianeGroup and the DLR respectively.

All simulations were carried out with an ideal gas equation of state, since the injection temperatures of both propellants were at around 270 K, rendering real-gas effects negligible. The computational domain in the RANS simulations was significantly reduced, in order to take advantage of the geometry's symmetry. The TUM and JAXA models consisted of 30°, corresponding to half injector in the outer row, whereas ArianeGroup, HIT and DLR chose 60°, equivalent to a full injector in the outer row. In order to resolve the heat transfer at the wall, all groups used meshes with $y^+ \approx 1$ values at the chamber and nozzle walls. The groups at TUM, HIT and JAXA utilized a two-layer model for the calculation of the turbulent viscosity, to account for the effect of walls in the standard $k-\epsilon$ model, whereas the DLR based their calculations on an SST $k-\omega$, therefore requiring no additional treatment of the wall boundary condition. In the case of the ArianeGroup setup, the low Reynolds $k-\epsilon$ model by Launder and Sharma was implemented, which modifies the standard $k-\epsilon$ model to allow its application to the entire fluid domain, including the near-wall region.

The main differences in the setup included the choice of combustion model and the corresponding Turbulence-Chemistry-Interaction (TCI). TUM, ArianeGroup and DLR implemented an adiabatic Flamelet model, which accelerates the computational time due to the tabulation of the chemistry occuring during pre-processing. For the TCI, a β-PDF for the mixture fraction was implemented by all three groups, whereas a Dirac function was used for the scalar dissipation PDF. JAXA used a laminar finite rate model, whereas the HIT calculations were based on the Eddy Dissipation Concept, which includes TCI. All groups used different combinations of the turbulent Prandtl (Pr_t) and turbulent Schmidt numbers (Sc_t) for the closure of the turbulent flux terms for heat and mass transfer respectively. Finally, the treatment of the transport properties is quite important for the correct estimation of the wall heat flux. For the calculation of viscosity and thermal conductivity of the individual species, the DLR group used Blottner curve fits, whereas the other groups implemented the Chapman-Enskog kinetic theory. ArianeGroup and JAXA implemented the equations using the Cantera package [2], which is based on CHEMKIN-II [3] for the transport properties. For the mixture rules, all groups' calculations were based on the Wilke mixture rule, whereas DLR modified it with the Herning-Zipperer mixing rule. A detailed summary of the settings is given in Table 1.

The boundary conditions used for the simulations were identical among the five groups. For the inlets, the mass flow of fuel and oxidizer were prescribed for the inner and outer injectors, whereas the nozzle exhaust was defined as a pressure outlet. In the case of the inlets, the computational domain of ArianeGroup did not include the injector elements, whereas they were resolved in the remaining four cases. For the calculation of the heat flux at the chamber and nozzle wall, a temperature profile was applied, coming from the experimental data. Due to the absence of experimental temperature measurements directly on the hot gas wall, the thermocouple data at 0.7 and 1mm were used. The resulting profile is shown in Fig. 2.

Groups	TUM	ArianeGroup	HIT	JAXA	DLR
Code	ANSYS Fluent	Rocflam3	ANSYS Fluent	CRUNCH-CFD	TAU
Equations	RANS	RANS	RANS	RANS	RANS
Solver	pressure based coupled	pressure based SIMPLE	pressure based coupled	density based	density based
Domain	3D 30°	3D 60°	3D 60°	3D 30°	3D 60°
Grid cells	$2.9 \cdot 10^6$	$2.7 \cdot 10^6$	$1.3 \cdot 10^6$	$4.7 \cdot 10^6$	$1.4 \cdot 10^6$
Turbulence model	standard $k-\epsilon$ Launder et al. [4]	$k-\epsilon$ Launder-Sharma Launder et al. [5]	standard $k-\epsilon$ Launder et al. [4]	standard $k-\epsilon$ Launder et al. [4]	$k-\omega$ SST Menter et al. [6]
Wall treatment	$y^+ \approx 1$ two-layer model [7], [8]	$y^+ \approx 1$ low-Re (Launder-Sharma)	$y^+ \approx 1$ two-layer model [7], [8]	$y^+ \approx 1$ two-layer model [7]	$y^+ \approx 1$
Combustion model	Flamelet	Flamelet	Eddy Dissipation Concept	Finite rate	Flamelet
TCI	β-PDF	β-PDF	EDC	laminar	β-PDF
Chemistry	21 species, 97 reac. Slavinskaya et al. [9]	35 species, 217 reac. GRI 3.0 [10]	14 species, 18 reac. Dong et al. [11]	21 species, 97 reac. Slavinskaya et al. [9]	35 species, 217 reac. GRI 3.0 [10]
Pr_t/Sc_t	0.9/0.6	0.8/0.5	0.85/0.7	0.7/0.9	0.5/0.5
Thermodynamics	NASA polynomials	NASA polynomials	NASA polynomials	NASA polynomials	Partition functions [12], [13]
Transport properties species	Kinetic theory [14], [15]	Kinetic theory Cantera [2]	Kinetic theory [14], [15]	Kinetic theory [2], [14]	Blottner curve fits Gupta [16], Gordon [17]
Transport properties mixture	Wilke mixture rule [15], [18]	Wilke mixture rule [2], [18]	Wilke mixture rule [8], [15], [18]	Wilke mixture rule [2], [18]	Wilke and Herning-Zipperer [18], [19]
Injector resolved	Yes	No	Yes	Yes	Yes

Table 1 Summary of computational setups.

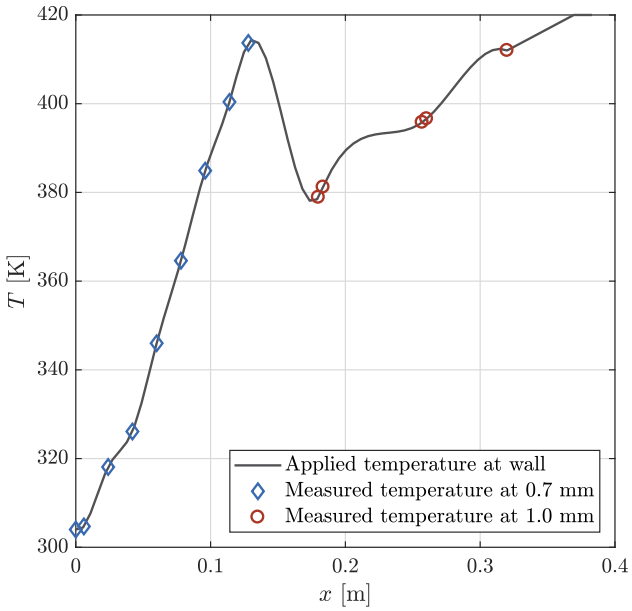

Fig. 2 Temperature profile at the chamber wall.

V. Results

The numerical results of all groups were first compared to the experimental data. For this comparison, focus was placed on the pressure and heat flux measurements available from the tests.

A. Pressure and average wall heat flux

The distributions of pressure and normalized pressure (normalized by the value of the pressure at the last sensor position) are presented in the left and right sub-figures of Fig. 3 respectively. It can be seen, that the HIT results are able to capture the pressure profile in high detail. The JAXA results lie approximately 0.4 bar or 2% above the experimental data, whereas the three flamelet approaches (TUM, ArianeGroup and DLR) underestimate the pressure by 0.4-0.7 bar. Previous studies on GCH_4/GOX rocket engine simulations with the Flamelet model have also indicated that the predicted pressure is usually lower than the experimental one. Further studies are carried out in order to detect the source of this discrepancy. The main assumption is that the Flamelet model with the PPDF TCI predicts a slightly lower chemical conversion of the propellants (incomplete combustion) leading to lower average temperatures and hence lower pressure.

Despite the slight departures from the absolute pressure level measured in the experiment, most groups are able to capture the pressure trend accurately. This is illustrated in the right sub-figure of Fig. 3, where the normalized profiles demonstrate the same curvature as the experimental measurements. Specifically, a slight increase is observed after the faceplate, followed by a monotonic pressure decrease due to the acceleration of the gas. At around 0.12 m from the injector plane, an inflection point is observed, which is visible also in the simulation results. Finally, a flattening of the pressure profile before the end of the chamber indicates that the combustion process is finished, and no further acceleration of the gas takes place. In the case of the DLR results, the pressure reduction and the inflection point take place further downstream, indicating a shift of the energy release towards the end of the combustion chamber.

The heat flux values from the RANS simulations and the experiments are shown in Fig. 4. The chamber consists of five individually cooled segments, four in the combustion chamber and one in the nozzle. The average heat flux for each one of the segments is available and plotted with a black line in Fig. 4. The RANS results have an angle dependency of the heat flux, due to the presence of a non-uniform injection (6 outer elements distributed along the perimeter). However, for the comparison with the experiment, the $\dot{q}$ values are averaged along the azimuthal direction and shown in the left sub-figure of Fig. 4. For a more quantitative comparison, the segment-averages are presented in the right sub-figure.

The profiles show some resemblances as far as the general trend is concerned, but also have some qualitative differences. The results from TUM show a monotonically increasing heat flux until the middle of the third segment. Downstream of this location, the heat flux decreases slightly, indicating the end of combustion and build-up of a thermal boundary layer. Finally, a sharp increase is present at the nozzle, which however under-predicts the measured value

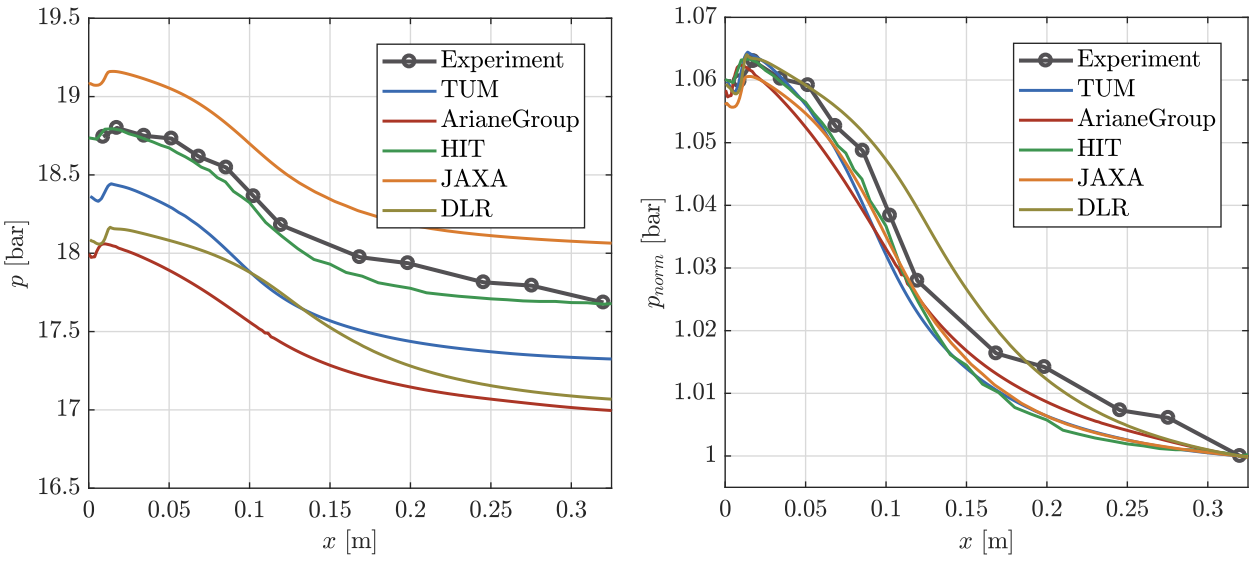

Fig. 3 Average pressure (left) and normalized average pressure (right) profile at the chamber wall.

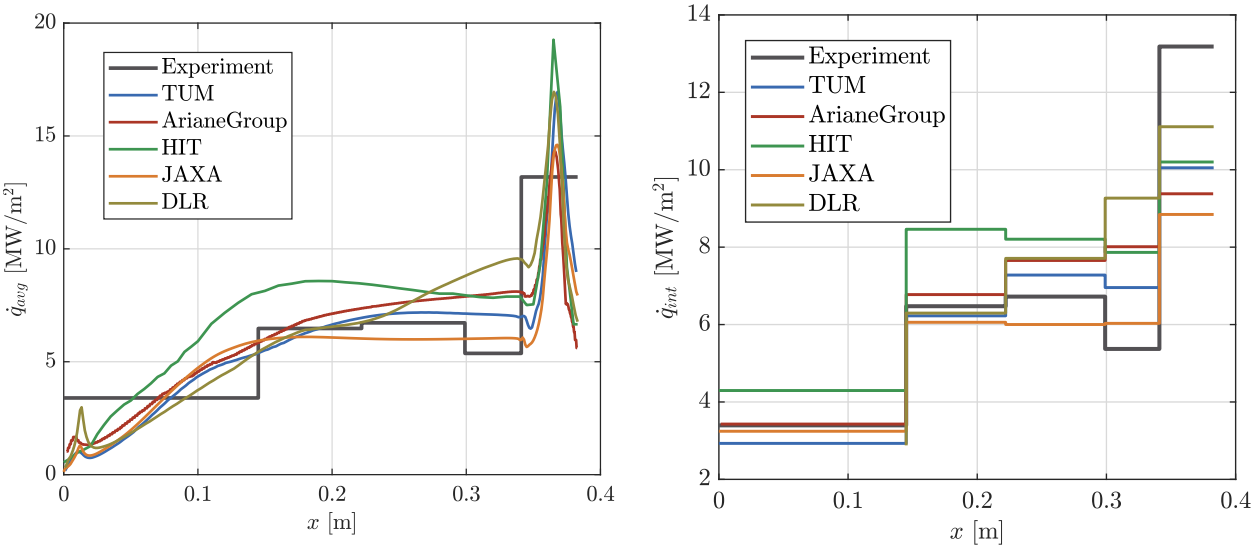

Fig. 4 Average heat flux along the perimeter (left) and integrated calorimetric heat flux (right) at the chamber wall.

by 30 %. The ArianeGroup results show a very similar profile, but with a higher heat flux value in the first segment, matching the experimental data better than TUM. Also, a shift of the combustion end further downstream is implied by a slight increase of the average heat flux in the final combustion chamber segment (D). Finally, the observed increase in the nozzle heat flux (compared to segment D) is less than in the experiment, leading to an underestimation of ca. 40%. The DLR results seem to match the ones of TUM and ArianeGroup up to the third segment, but then predict a sharp increase of the heat flux close to the nozzle, hinting on a shift of the energy release further downstream.

In the case of HIT, the average heat flux is slightly overestimated in the combustion chamber relative to the experiment and the other four simulations. The heat flux reaches a maximum in segment B and is then reduced up until the nozzle, indicating a complete combustion. Finally, the JAXA results predict a similar trend, with an increase of the heat flux up to segment B and a subsequent constant value till the end of the combustion chamber.

All five simulations have in common that the nozzle heat flux remains well underneath the experimental value. The explanation for this discrepancy was attributed to an inconsistency of the test data. It was established, that the coolant

mass flow in the nozzle was over-dimensioned, leading to a strong cooling of the nozzle material. This led to axial heat conduction between the segment D and segment N, causing energy that would be otherwise deposited into the water cycle of segment D, to end up in the water of segment N. Consequence of this heat transfer was the reduction of the measured heat flux in the last combustion chamber segment and a direct increase in the experimental heat flux of the nozzle. This point has been first demonstrated by Silvestri et al. [1], [20] and was independently shown also by Rahn et al. [21], Perakis et al. [22] and Daimon et al. [23]. For that reason, absolute value comparisons of the nozzle heat flux were not carried out between the simulation and the test data. Direct comparisons stemming from fully conjugate coupled or one-way coupled simulations of the hot gas and the chamber structure can be found in the references listed above.

B. Azimuthal heat flux profiles

Apart from the average heat flux, the local heat flux distribution along the azimuthal direction of the chamber wall was examined at different locations from the injector plane. The results for 10 mm, 20 mm, 30 mm, 40 mm, 50 mm, 100 mm, 200 mm and 300 mm are illustrated in Fig. 5. An angle of $\theta = 0°$ represents the location directly above the injector element in the outer row, and $\theta = \pm 30°$ the symmetry plane between two adjacent elements.

The differences between the different solutions are prominent along the whole length of the chamber and therefore each groups solution is described briefly. To facilitate the discussion of the differences, the temperature field at 10 mm, 20 mm and 30 mm from the faceplate as well as the vorticity along the x direction are plotted in Fig. 6 and Fig. 7 respectively. The vorticity is chosen since it was found that the secondary flow patterns play a role in the circumeferencial temperature and heat flux.

1. TUM

Close to the faceplate (within the first 20 mm), the heat flux appears to have a clear maximal value at 0°, i.e. directly above the outer injector element and a minimum at ±30°. Further downstream however, a shift in the position of the maximum heat flux seems to occur. Specifically, starting at 30 mm, a second local maximum appears at $\pm \sim 15°$, which becomes an absolute maximum after 50 mm. The heat flux directly above the injector element at 0° and between the elements at ±30° show almost the same value. For positions after the initial mixing (200 mm), the heat flux has almost a plateau between −15° and 15° with minima at ±30°. Finally, close to the end of the combustion chamber, the temperature field seems to be fully homogeneous which leads to a uniform heat flux profile.

In the near injector region, the flames are not fully developed and the initial hydrodynamic mixing of the propellants plays a big role. Here the interaction between the injectors is not strong, each injector can be mainly considered as independent. Hence, the maximum temperature and heat flux are achieved at the angular position where the injectors are located. The observed shift of heat flux maximum between $\sim$ 30 and $\sim$ 100 mm implies that after a specific point in the chamber, the interaction between the injectors is intensified, leading to a second zone of hot gas between the injectors.

This is seen in Fig. 6 and Fig. 7. A notable hot temperature point is created at ±15° and the reason appears to be a strong vortex system at this position. This leads to the distortion of the temperature field and an increased heat transfer coefficient at this angular position. A finer resolution of the near-injector region and a simulation of a larger computational domain (120° instead of 30°) did not eliminate this phenomenon as mentioned in Perakis et al. [22].

2. ArianeGroup

After an initial flat profile close to the injector plane, starting from around 30 mm, a maximum develops directly above the injector element. The position of the maximal heat flux remains unaltered over the whole length of the chamber at 0°. For positions close to the end of combustion chamber, the circumferential variation of the heat flux remains visible, with a difference of 2 $\mathrm{MW/m^2}$ between maximal and minimal value.

By examining the flowfield, one understands that following the propellant injection zone at the faceplate, a secondary flow pattern forms in the region between the stoichiometric zone and the combustion chamber wall. This phenomenon drives the radial expansion of the outer flame and initiates a respective flattening at the 0° position above the center of the injection element.

It is found that the secondary flow patterns are dissipated quite fast and hence the azimuthal and radial velocity components in the numerical solution are small compared to the axial main flow direction magnitude. Thereby, due to the low ratio of axial to non-axial velocity magnitude, a subsequently weak effect of the secondary pattern on the global flow field is present. As a consequence, the driving force of the flame deformation has a negligible impact for a large

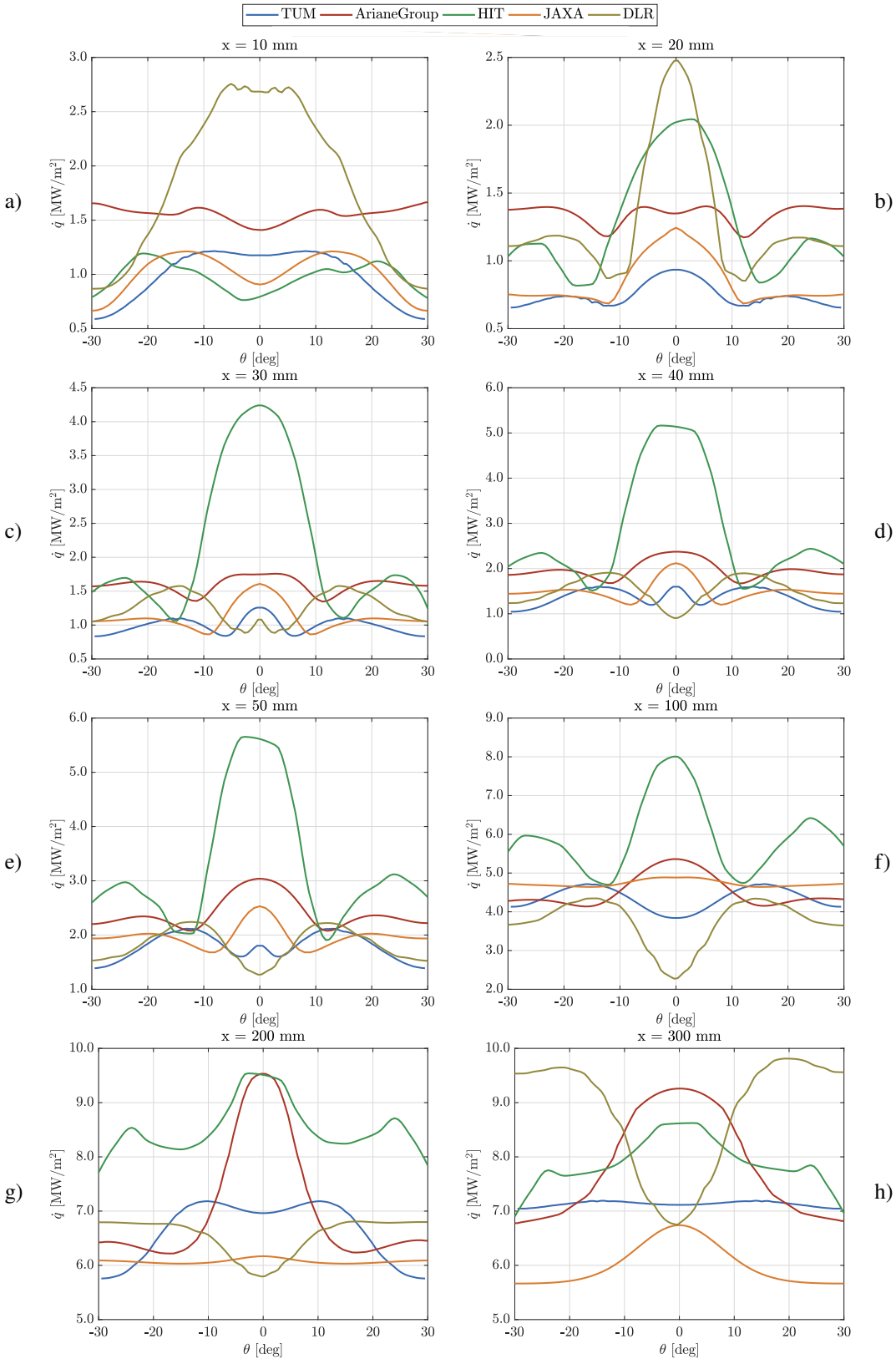

Fig. 5 Azimuthal heat flux profile at the axial positions x=10 mm, 20 mm, 30 mm, 40 mm, 50 mm, 100 mm, 200 mm, 300 mm.

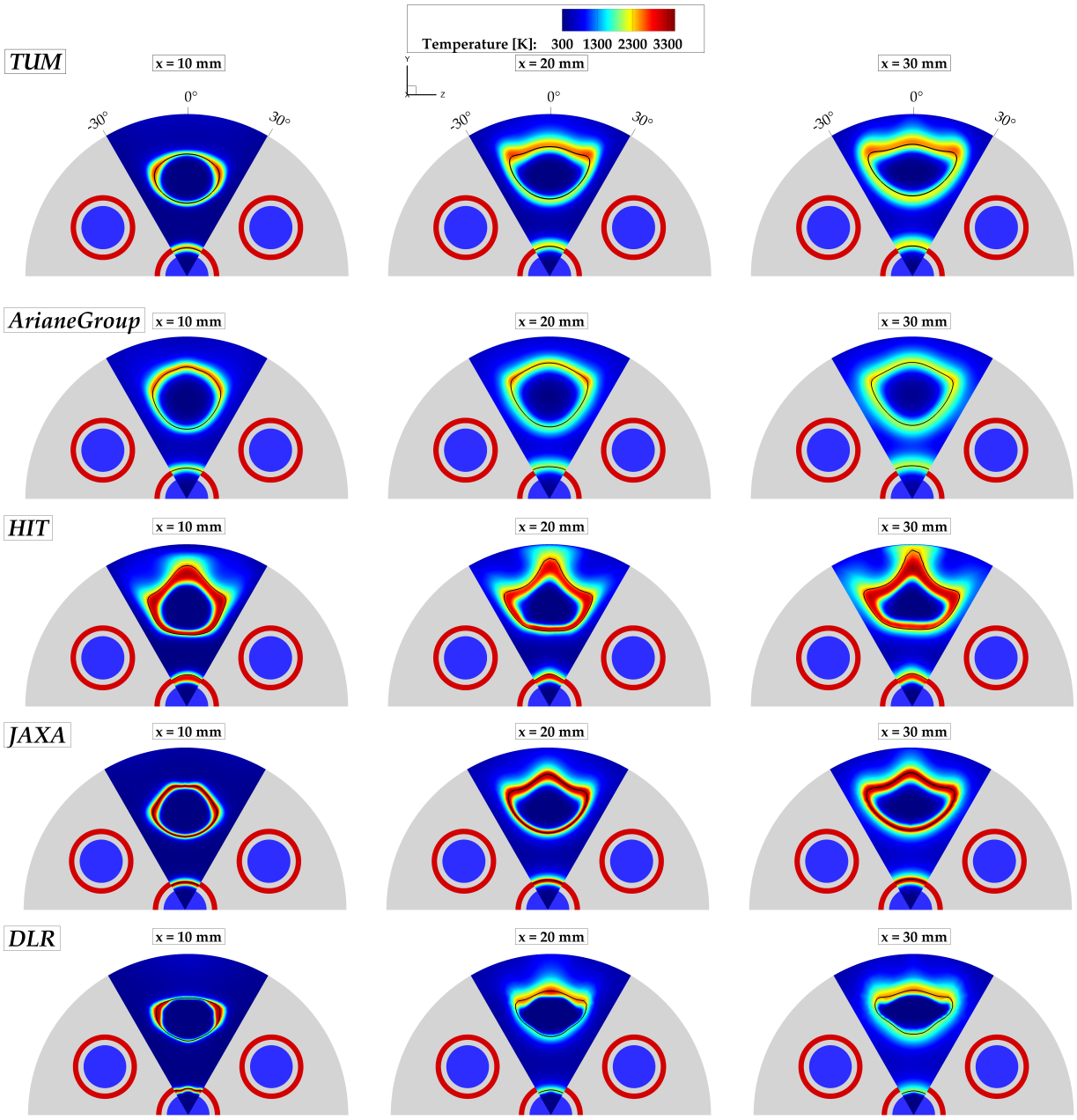

Fig. 6 Temperature contour plots at x=10 mm, 20 mm and 30 mm. The line represents the stoichiometric composition.

share of the combustion chamber domain. This rapid weakening after the injection zone ensures the manifestation of the initial flame position and its respective circumferential structure leading to the observed temperature distribution with higher values at the 0° position of the injection element and lower values in the intermediate zones at ± 30° in Fig 6.

Increasing the grid resolution and therefore the number of computational cells present in the respective secondary flow region for the numerical simulation with Rocflam3 does not have a significant impact on the discussed results.

3. HIT

Similar to the solution of ArianeGroup, the HIT heat flux profile shows a maximum at the 0° position, which establishes itself right after the initial recirculation zone (~ 20 mm). This maximum directly above the injector remains

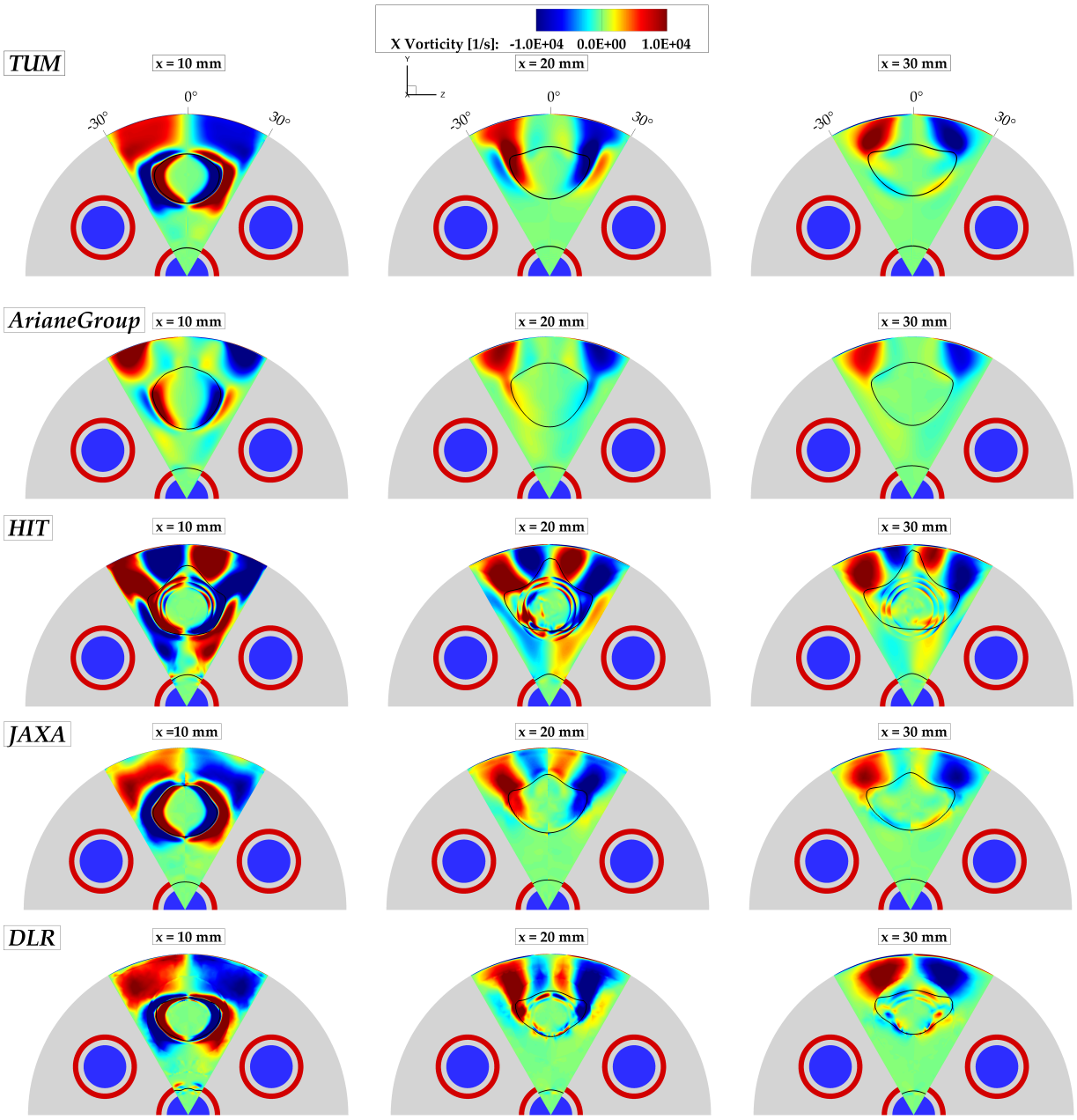

Fig. 7 Vorticity contour plots at x=10 mm, 20 mm and 30 mm. The line represents the stoichiometric composition.

throughout the length of the chamber and a very large difference between the maximal and minimal heat flux values is predicted, reaching up to 3 MW/m^2 between 30 mm and 100 mm.

This very prominent maximum at the injector angular position is a direct consequence of the significant vertical flame stretching observed in Fig. 6. Even at the 10 mm plane, it appears that the flame expands rapidly towards the wall leading to a direct rise of the local heat input into the wall. This effect also explains the increased average heat flux from Fig. 4.

As for the origin of the strong flame stretch, a powerful vortex system has been identified as shown in Fig. 7. Specifically, from -10° to 10°, a secondary flow pattern seems to be feeding hot gas from the shear layer directly onto the wall, which increases the local heat transfer. The intensity of the secondary flows (magnitude of the vorticity) seems to be higher than in all the other solutions and its damping is also reduced, which explains why the pattern remains

unaltered until the end of the chamber.

A refinement of the mesh is planned in order to understand if the source of those strong vortices is the low cell number in the HIT solution.

4. JAXA

Similar to the other groups, the JAXA solution is predicting the formation of a maximum in the heat flux profile following the initial recirculation zone (after 20 mm). This maximum prevails until around 100 mm, where the heat flux profile attains a homogeneous, almost constant distribution. Further downstream of this point, the maximum seems to come into existence again but remains constraint in magnitude. For all planes examined, the difference between maximal and minimal heat flux does not exceed 1 MW/m^2.

The temperature field shows that a slight stretch of the flame similar to the one in the HIT solution is present after the first 10 mm of the flow. The creation of this vertical flame distortion is fed by a vortex system at 0°. The main difference to the HIT solution is the intensity of this secondary flow, which is reduced approximately by 40% and the fact that it is damped out pretty fast, since it is shown to disappear at 30 mm. This fast damping of the radial and tangential velocity components explains also why the azimuthal heat flux variation remains small in magnitude.

5. DLR

Similar to the TUM profile, the DLR solution also predicts a shift in the position of the maximal heat flux. In the upstream section of the combustor, the azimuthal peak of the surface heat flux is correlated to the flame position as illustrated by the cut plot at x = 10 mm. hence a maximum is observed at 0° already at 10 mm. This increased heat flux directly above the injector remains present for the first 20 mm but is replaced by a rapid change to a local minimum starting from 30 mm. For all remaining axial positions up until the end of the chamber, the maximal heat flux is observed at $\pm \sim 20°$ with the above-injector heat flux being significantly lower (up to 3 MW/m^2 difference).

The presence of a strong vortex system at between $\pm 10 - 20°$ is responsible for this behavior. Specifically the vortex is built after 20 mm and has low damping close to the wall, thereby increasing the surface heat flux. The temperature profile confirms this assumption. Similar to the TUM results, an initial tangential expansion of the flame is observed. As soon as the interaction between the neighboring injectors becomes stronger (20 mm), this initial lateral expansion is pushed towards the wall and increases the heat load.

6. Comparison

The differences between the individual solutions can be attributed to three separate features of the setups:

- The combustion model
- The turbulence model
- The injector resolution

The DLR and the TUM setups produce a local heat flux minimum at 0°, but the effect is much more prominent in the DLR case. They are both using an adiabatic Flamelet model for the combustion. The main origin for the observed difference in the solutions is believed to be the turbulence model ($k - \omega$ SST vs standard $k - \epsilon$). The TUM simulation was also run using the SST model as shown in [22], where it was shown that the azimuthal heat flux variation is intensified compared to the $k - \epsilon$.

The third setup utilizing the Flamelet model is the ArianeGroup one. The numerical setup for the Rocflam3 simulation differs from the other research groups as the upstream parts of the injection elements are not resolved. Instead, the standard approach of mapping the geometric dimensions of the injector to the block-structured grid is followed. Thereby, the mass flow inlet boundary condition is enforced directly at the combustion chamber faceplate for computational cell surfaces, whose center point is situated within the area defined by the central oxidizer post and annular fuel sleeve. For this inflow condition, the radial and azimuthal velocity components are assumed to be zero. This can give rise to a different turbulence kinetic energy and secondary flow field close to the faceplate, leading to the different heat flux profiles. Due to the fast damping of the secondary vortices, this initial difference in the heat flux profile is transported downstream.

The HIT and JAXA results on the other hand implement a finite rate approach (EDC for the HIT and Laminar Finite Rate for JAXA). The two solutions predict both a maximum heat flux value directly above the injector for the full chamber length. The main difference is the magnitude for the circumferential heat flux variation, which is strongly amplified in the HIT case. Further investigations are needed to resolve the origin of this disagreement but one candidate

is that a refinement may be needed in the HIT grid, which could be the cause for the low damping of the vortices and the high heat flux input at 0°.

Finally, the observed differences between the three Flamelet approaches (TUM, DLR, ArianeGroup) and the Finite Rate ones (HIT, JAXA) could be traced back to the Turbulence-Chemistry-Interation. The first group uses beta-PDF whereas the second one has no direct TCI. This explains the much higher temperatures and the different flow patterns in the recirculation zone. The HIT and JAXA solutions also predict a second, strong recirculation zone at 0° (at least for the first planes close to the faceplate), which is not so prominent in the Flamelet solutions.

Currently, no experimental values are available for a more detailed comparison and only the average wall heat flux is known. Measurements of the wall temperature at different azimuthal positions have been taken and were presented by Silvestri et al. [20]. The results of the local temperature variation are shown in Fig. 8 and the plotted T_{var} is defined as the difference between the local and the circumferentially average temperature.

$$T_{var} = \frac{T_{thermo} - \frac{1}{N}\sum_i^N T_{thermo,i}}{\frac{1}{N}\sum_i^N T_{thermo,i}} \cdot 100 \tag{1}$$

N stands for the number of the thermocouples available in circumferential direction.

The angular positions 0° and 60° in Fig. 8 are aligned with the positions of the central axes of the injector elements in the outer row, whereas 30° and 90° correspond to the positions in the symmetry plane between injectors. The measurements at 30° are copied to the -30° position and the 60° ones to the 120° position for visualization reasons.

The experimental measurements demonstrate a slight asymmetry in the measurements, with the temperatures above the injector at 0° having much higher temperatures compared to 60°. In both positions however it is observed that although a high temperature is attained at the positions close to the faceplate (0-90 mm), a lower temperature is measured in positions further downstream (100-110 mm). At the same time, the between-injector positions show a similar pattern. Initially, a temperature below the average one is measured and at 110 mm, an increase in temperature and hence heat flux is observed.

This behavior is similar to the one predicted by the TUM and DLR calculations, where the local heat flux above the injector showcased a minimum. Nevertheless, this experimental trend still remains to be further analyzed. An inverse heat flux evaluation method is planned to be applied to the experimental data in order to obtain quantitative data which can be compared with the CFD simulations.

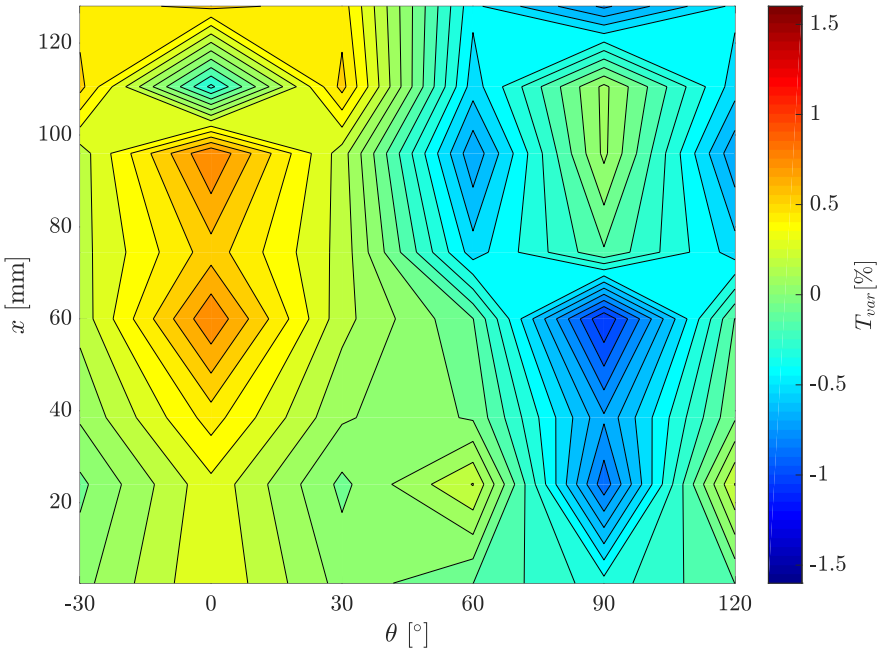

Fig. 8 Measured temperature variation from the mean value (modified from Silvestri et al. [20].

VI. Conclusion

Five independent groups from Germany, Japan and China have performed 3D RANS simulations of a 7 element rocket combustor operated with gaseous oxygen and gaseous methane. The simulation results of the research groups have been compared to each other and to the experimental data. Good agreement with the pressure results and heat flux level in the combustion chamber were observed. In general the groups using tabulated chemistry approaches for the combustion modeling (Flamelet) predicted a lower combustion pressure than the experiment, whereas the finite rate based methods produced results which either exceeded or matched the absolute wall pressure.

In the case of the nozzle heat flux, a significant underestimation of the calculated results was found. The large deviation from the experiment was attributed to the high water mass flow rate in the nozzle stemming from the experimental setup. This induced a large axial thermal gradient and led to a systematic error in the evaluation of the heat flux in the final two segments.

Apart from the average heat flux profile, the local heat transfer at the wall is very important for the correct design of the combustion chamber, since the maximum local heat load often exceeds the average one. The heat flux profile along the angle was therefore also examined. Important discrepancies between the results of the individual groups were seen. Specifically, a shift in the location of the local minimum was observed for two of the five groups. Also, some groups predicted a flattening of the heat flux profile at downstream positions, whereas others maintained a high variation in the profile. By examining the temperature and vorticity fields close to the faceplate, some light was shed into the observed disagreement. Specifically it was found that the local secondary flows stemming from the single injector's recirculation zone and from the injector/injector interaction significantly influence the local turbulent heat transfer and can drastically change the way the flame is stretched. Important factors which were found to affect the circumferential heat flux profile are the choice of turbulence model, the turbulence-chemistry interaction and the resolution of the injector.

Finally, the state of the art simulation setups from academia, research institutes and industry were presented. Although the weaknesses of RANS models are known, the design and verification process of multi- and full-scale engines heavily relies on their use in CFD simulations, since more elaborate models such as LES are still computationally expensive. The significant difference in the obtained results proves that especially for the simulation of methane/oxygen engines, further modeling is needed to accurately capture the physical phenomena occurring in the thrust chamber.

Acknowledgments

Authors N. Perakis and O. Haidn gratefully acknowledge the Gauss Centre for Supercomputing e.V. (www.gauss-centre.eu) for funding this project by providing computing time on the GCS Supercomputer SuperMUC at Leibniz Supercomputing Centre (www.lrz.de). Financial support has been provided by German Research Foundation (Deutsche Forschungsgemeinschaft-DFG) in the framework of the Sonderforschungsbereich Transergio 40.

Authors D. Rahn and D. Eiringhaus acknowledge the financial support granted by the Bayerische Forschungsstiftung within the project „Umweltfreundliche Treibstoffkombination LOX/Methan“ and on the ArianeGroup side within the national technology program TARES 2020 sponsored by the German Space Agency, DLR Bonn, under contract No. 50RL1710.

References

[1] Silvestri, S., Celano, M. P., Schlieben, G., and Haidn, O. J., "Characterization of a Multi-Injector GOX-GCH4 Combustion Chamber," *Joint Propulsion Conference, JPC*, 2016.

[2] Goodwin, D. G., Moffat, H. K., and Speth, R. L., "Cantera: An Object-oriented Software Toolkit for Chemical Kinetics, Thermodynamics, and Transport Processes," `http://www.cantera.org`, 2017. doi:10.5281/zenodo.170284, version 2.3.0.

[3] Kee, R. J., Rupley, F. M., and Miller, J. A., "Chemkin-II: A Fortran chemical kinetics package for the analysis of gas-phase chemical kinetics," Tech. rep., Sandia National Labs., Livermore, CA (USA), 1989.

[4] Launder, B. E., and Spalding, D. B., *Mathematical models of turbulence*, Academic press, 1972.

[5] Launder, B., and Sharma, B., "Application of the energy-dissipation model of turbulence to the calculation of flow near a spinning disc," *Letters in heat and mass transfer*, Vol. 1, No. 2, 1974, pp. 131–137.

[6] Menter, F. R., "Two-equation eddy-viscosity turbulence models for engineering applications," *AIAA journal*, Vol. 32, No. 8, 1994, pp. 1598–1605.

[7] Wolfshtein, M., "The velocity and temperature distribution in one-dimensional flow with turbulence augmentation and pressure gradient," *International Journal of Heat and Mass Transfer*, Vol. 12, No. 3, 1969, pp. 301–318.

[8] Fluent, A., "Ansys fluent theory guide," *ANSYS Inc., USA*, Vol. 15317, 2011, pp. 724–746.

[9] Slavinskaya, N., Abbasi, M., Starcke, J.-H., Mirzayeva, A., and Haidn, O. J., "Skeletal Mechanism of the Methane Oxidation for Space Propulsion Applications," *52nd AIAA/SAE/ASEE Joint Propulsion Conference*, 2016, p. 4781.

[10] Smith, G. P., Golden, D. M., Frenklach, M., Moriarty, N. W., Eiteneer, B., Goldenberg, M., Bowman, C. T., Hanson, R. K., Song, S., Gardiner Jr, W. C., et al., "GRI 3.0 Mechanism," *Gas Research Institute (http://www. me. berkeley. edu/gri_mech)*, 1999.

[11] Dong, G., Huang, Y., and CHEN, Y.-l., "Study of Effects of Different Chemical Reaction Mechanisms on Computation Results for Methane Jet Turbulence Diffusion Flame," *Journal of Fuel Chemistry and Technology*, Vol. 28, No. 1, 2000, pp. 49–54.

[12] Glushko, V., "Thermodynamical properties of individual species," *Hemisphere*, 1989.

[13] Iii, R. J., "NIST Computational Chemistry Comparison and Benchmark Database (CCCBDB)," *NIST Standard Reference Database*, , No. 101, 2017. URL `http://cccbdb.nist.gov/`.

[14] Hirschfelder, J., Curtiss, C., and Bird, R., "Molecular Theory of Gases and LiquidsJohn Wiley," *New York*, 1954.

[15] Bird, R. B., Stewart, W. E., and Lightfoot, E. N., "Transport phenomena. 1960," *Madison, USA*, 1960.

[16] Gupta, R. N., Yos, J. M., Thompson, R. A., and Lee, K.-P., "A review of reaction rates and thermodynamic and transport properties for an 11-species air model for chemical and thermal nonequilibrium calculations to 30000 K," 1990.

[17] Gordon, S., and McBride, B. J., *Computer program for calculation of complex chemical equilibrium compositions and applications*, Vol. 1, National Aeronautics and Space Administration, Office of Management, Scientific and Technical Information Program, 1994.

[18] Wilke, C., "A viscosity equation for gas mixtures," *The journal of chemical physics*, Vol. 18, No. 4, 1950, pp. 517–519.

[19] Herning, F., "Beitrag zur Berechnung der Zähigkeit technischer Gasgemische aus den Zähigkeitswerten der Einzelbestandteile..." Ph.D. thesis, Karlsruhe (Technische Hochschule), 1935.

[20] Silvestri, S., Kirchberger, C., Gregor, S., Celano, M. P., Schlieben, G., and Haidn, O. J., "Experimental and Numerical Investigation of a Multi-Injector GOX-GCH4 Combustion Chamber," *International Symposium on Space Technology and Science, ISTS, Japan*, 2017.

[21] Rahn, D., Eiringhaus, D., Riedmann, H., Behr, R., and Haidn, O. J., "Characterization of an adiabatic Flamelet combustion model for gaseous CH4/O2 combustion in rocket thrust chambers," *Space Propulsion Conference, Sevilla, Spain*, 2018.

[22] Perakis, N., Rahn, D., Eiringhaus, D., and Haidn, O. J., "Heat transfer and combustion simulation of a 7-element GOX/GCH4 rocket combustor," *Joint Propulsion Conference, JPC, Cinncinati OH, USA*, 2018.

[23] Daimon, Y., Negishi, H., Silvestri, S., and Haidn, O., "Conjugated Combustion and Heat Transfer Simulation for a 7 element GOX/GCH4 Rocket Combustor," *Joint Propulsion Conference, JPC, Cincinnati OH, USA*, 2018.